The Astronomical Journal, 168:211 (10pp), 2024 November https://doi.org/10.3847/1538-3881/ad77d2

Discovery of 118 New Ultracool Dwarf Candidates Using Machine-learning Techniques

Hunter Brooks[1,2], Dan Caselden[3], J. Davy Kirkpatrick[4], Yadukrishna Raghu[5], Charles A. Elachi[6], Jake Grigorian[7], Asa Trek[5], Andrew Washburn[5], Hiro Higashimura (東村滉)[8], Aaron M. Meisner[2], Adam C. Schneider[9], Jacqueline K. Faherty[3], Federico Marocco[4], Christopher R. Gelino[4], Jonathan Gagné[10,11], Thomas P. Bickle[5,12], Shih-Yun Tang[13,14], Austin Rothermich[3,5,15,16], Adam J. Burgasser[17], Marc J. Kuchner[18], Paul Beaulieu[5], John Bell[5], Guillaume Colin[5], Giovanni Colombo[5], Alexandru Dereveanco[5], Deiby Pozo Flores[5], Konstantin Glebov[5], Leopold Gramaize[5], Les Hamlet[5], Ken Hinckley[5], Martin Kabatnik[5], Frank Kiwy[5], David W. Martin[5], Raúl F. Palma Méndez[5], Billy Pendrill[5], Lizzeth Ruiz[5], John Sanchez[5], Arttu Sainio[5], Jörg Schümann[5], Manfred Schonau[5], Christopher Tanner[5], Nikolaj Stevnbak[5], Andres Stenner[5], Melina Thévenot[5], Vinod Thakur[5], Nikita V. Voloshin[5], and Zbigniew Wędracki[5]

The Backyard Worlds: Planet 9 Collaboration

[1] Department of Astronomy and Planetary Science, Northern Arizona University, Flagstaff, AZ 86011, USA
[2] NSF National Optical-Infrared Astronomy Research Laboratory, 950 N. Cherry Avenue, Tucson, AZ 85719, USA
[3] Department of Astrophysics, American Museum of Natural History, Central Park West at 79th Street, New York, NY 10024, USA
[4] IPAC, Mail Code 100-22, Caltech, 1200 E. California Boulevard, Pasadena, CA 91125, USA
[5] Backyard Worlds: Planet 9
[6] Seaver College, Pepperdine University, Malibu, CA 90263, USA
[7] University of Southern California, University Park Campus, Los Angeles, CA 90089, USA
[8] Earl of March Intermediate School, 4 The Pkwy, Kanata, ON K2K 1Y4, Canada
[9] United States Naval Observatory, Flagstaff Station, 10391 West Naval Observatory Road, Flagstaff, AZ 86005, USA
[10] Planétarium de Montrál, Espace pour la Vie, 4801 av. Pierre-de Coubertin, Montréal, Québec, Canada
[11] Trottier Institute for Research on Exoplanets, Université de Montréal, Département de Physique, C.P. 6128 Succ. Centre-ville, Montréal, QC H3C 3J7, Canada
[12] School of Physical Sciences, The Open University, Milton Keynes, MK7 6AA, UK
[13] Department of Physics and Astronomy, Rice University, 6100 Main Street, Houston, TX 77005, USA
[14] Lowell Observatory, 1400 West Mars Hill Road, Flagstaff, AZ 86001, USA
[15] Department of Physics, Graduate Center, City University of New York, 365 5th Avenue, New York, NY 10016, USA
[16] Department of Physics and Astronomy, Hunter College, City University of New York, 695 Park Avenue, New York, NY 10065, USA
[17] Department of Astronomy & Astrophysics, UC San Diego, La Jolla, CA, USA
[18] NASA Goddard Space Flight Center, Exoplanets and Stellar Astrophysics Laboratory, Code 667, Greenbelt, MD 20771, USA
Received 2024 August 12; revised 2024 August 24; accepted 2024 August 26; published 2024 October 17

Abstract

We present the discovery of 118 new ultracool dwarf candidates, discovered using a new machine-learning tool, named `SMDET`, applied to time-series images from the Wide-field Infrared Survey Explorer. We gathered photometric and astrometric data to estimate each candidate's spectral type, distance, and tangential velocity. This sample has a photometrically estimated spectral class distribution of 28 M dwarfs, 64 L dwarfs, and 18 T dwarfs. We also identify a T-subdwarf candidate, two extreme T-subdwarf candidates, and two candidate young ultracool dwarfs. Five objects did not have enough photometric data for any estimations to be made. To validate our estimated spectral types, spectra were collected for two objects, yielding confirmed spectral types of T5 (estimated T5) and T3 (estimated T4). Demonstrating the effectiveness of machine-learning tools as a new large-scale discovery technique.

Unified Astronomy Thesaurus concepts: Brown dwarfs (185); Subdwarf stars (2054); Low mass stars (2050)

Materials only available in the online version of record: machine-readable table

1. Introduction

The continued discovery of new brown-dwarf candidates enables a better understanding of the initial mass function at low masses, and modeling of the formation and evolution of local stellar populations (F. Dantona & I. Mazzitelli 1986). With recent discoveries and advancements in the study of exoplanets, it has become increasingly clear that brown dwarfs and large gaseous exoplanets have similar characteristics (J. K. Faherty et al. 2021). Therefore, increasing the variety and number of identified brown dwarfs results in a more diverse set of analogs against which to compare exoplanets.

One method to discover large numbers of brown dwarfs is to survey catalogs for objects with colors similar to those of known brown dwarfs. For example, J. D. Kirkpatrick et al. (2011) employed this technique using early data from the Wide-field Infrared Survey Explorer (WISE; E. L. Wright et al. 2010), focusing on the W1 − W2 color to identify potential brown dwarfs and applying a criterion to remove extragalactic sources: $W1 - W2 > 0.96\,(W2 - W3) - 0.96$. However, purely imaging-based discovery can still lead to sample contamination from extragalactic sources, even with removal criteria in place.

Another approach to brown-dwarf discovery is to survey based on proper motion, which helps exclude extragalactic sources as contaminants. Several proper motion surveys have been conducted across various telescopes, an example includes using WISE imaging due to the long time baseline of the WISE/NEOWISE mission (J. D. Kirkpatrick et al. 2014, 2016; K. L. Luhman 2014; A. C. Schneider et al. 2016; M. J. Kuchner et al. 2017; J. J. Greco et al. 2020; T. Kota et al. 2022, and others). However, a search strategy that focuses on proper motion may miss objects whose space motions are primarily along the line of sight. Moreover, for brown dwarfs at further distances, detecting its proper motions will be increasingly difficult unless the time baseline or motion is large.

This paper applies a novel proper motion detection technique to discover a large sample of faint, fast-moving objects, using a new convolutional neural network model called SMDET was developed (D. Caselden et al. 2020 and Caselden et al. 2024, in preparation). SMDET's technique and the new candidate sample are described in Section 2. Photometry and astrometry for each object were gathered as described in Section 3. Section 4 discusses photometric spectral-type estimation, for which we use the photo-type method discussed in N. Skrzypek et al. (2015, 2016). With these photometric spectral types, we estimate distances and tangential velocities in Section 5. A handful of objects, not following the general color trends laid out in J. D. Kirkpatrick et al. (2021) for M, L, T, and Y dwarfs, found to be candidate subdwarfs as discussed in Section 6. We discuss the identification of possible young ultracool dwarfs in our study in Section 7, and the limitations of our study in Section 8. Our main results are summarized in Section 9.

2. Methods For Discovering New Ultracool Dwarf Candidates

2.1. SMDET

Brown dwarfs are challenging to detect because they are inherently dim and emit primarily at infrared wavelengths. Many known brown dwarfs were discovered using infrared imaging, including WISE data (e.g., M. C. Cushing et al. 2011; M. J. Kuchner et al. 2017; A. M. Meisner et al. 2020a; J. D. Kirkpatrick et al. 2021). These brown dwarfs are generally nearby and, as a result, predominantly exhibit high proper motions. However, it has proven relatively challenging to discover high proper motion brown dwarfs ($\geqslant 0\farcs35\ \mathrm{yr}^{-1}$) significantly fainter than the WISE W2 single-exposure detection limit of W2 = 14.5 Vega mag (J. K. Faherty et al. 2009 and G. Bihain & R.-D. Scholz 2016). This limitation motivated us to search for such brown dwarfs using SMDET (D. Caselden et al. 2020, 2024, in preparation), a neural network that detects faint, fast-moving objects in WISE images.

The unWISE project reprocessed WISE exposures into coadds preserving the native WISE angular resolution (A. M. Meisner et al. 2018). SMDET was trained with synthetic objects added to unWISE time series coadds. Preliminary sky region rankings and segmented time series images were produced by SMDET across the entire sky with unWISE time series coadds. Sky regions were ranked according to the presence of faint, fast objects. The segmented time series images indentify which pixels in the input capture 1% or more of a faint, fast object's flux. For additional information regarding the backbone of SMDET, see D. Caselden et al. (2020, 2024, in preparation).

2.2. Human Verification

After the training of SMDET, candidates drawn from regions with the highest scores were given to citizen scientist collaborators to visually scrutinize for the presence of real motion objects, distinguishing them from artifacts like diffraction spikes and ghosts. During the process of visually vetting SMDET candidates, 1730 real proper motion objects and 10,170 WISE artifacts, diffraction spikes, and ghosts were identified out of 11,900 SMDET candidates inspected by our team.

2.3. Filtering Out Known Objects

We searched the SIMBAD Astronomical Database (M. Wenger et al. 2000) and the VizieR Catalog Access Tool (R. M. Cutri et al. 2021) to determine which of the 1730 confirmed proper motion objects might be previously cataloged. We used a search radius of $1\farcm0$ and followed up with visual confirmation of the cross-matched object with our real motion objects, resulting in 232 previously uncataloged sources.

After exploring the literature, we searched Gaia Data Release 3 (Gaia Collaboration et al. 2023) to eliminate objects that matched Gaia sources, as our focus is on cold brown dwarfs that are unlikely to be detectable with Gaia. We used the Wide-field Retrieval of Astrodata Program (hereafter, WRAP; H. Brooks et al. 2023) Gaia search feature with a radius of $150''$. The large search radius was necessary to confirm objects that are in crowded fields. This left 118 new high proper motion ultracool dwarf candidates. These candidates are presented in Table 1 and their sky distribution is illustrated in Figure 1. The plot indicates that there is no apparent bias toward either the galactic plane or the poles. Note that many of these candidates were independently discovered as moving object candidates through the Backyard Worlds: Planet 9 citizen science project (M. J. Kuchner et al. 2017). Volunteer citizen scientists who also identified these objects are included in the "Discoverers" column in Table 1.

3. Photometry and Astrometry

Archival photometric data were collected for the 118 discoveries to help with source characterization. The catalogs used to gather the photometry were CatWISE2020 (F. Marocco et al. 2021), the AllWISE Source Catalog (hereafter, AllWISE; R. M. Cutri et al. 2021), the VISTA Hemisphere Survey[19] (hereafter, VHS; N. J. G. Cross et al. 2012), the UKIRT Infrared Deep Sky Survey Large Area Survey Data Release 9/UKIRT Hemisphere Survey[20] (hereafter, UKIDSS LAS DR9/UHS; A. Lawrence et al. 2007 and S. Dye et al. 2018), and PanSTARRS Data Release 2 (hereafter, PanSTARRS DR2; K. C. Chambers et al. 2016). Any catalogs associated rejection table was not used during the query for photometric data. The associated photometric bands used in our analysis were W1 and W2 from CatWISE2020, W3 and W4 from AllWISE, J and K_s from VHS, J and K_{MKO} from UKIDSS LAS DR9/UHS, and g_{ps}, r_{ps}, i_{ps}, z_{ps}, y_{ps} from PanSTARRS DR2. All photometric data are provided in Table 1.

To gather these data and their associated uncertainties, we used WRAP with a search radius of $150''$, this large search radius is to aid visual confirmation in crowded fields. We confirmed the photometric data visually using WRAP's catalog overlay feature, which overlays catalog data on the relevant catalog imaging. WRAP also provides a WiseView (D. Caselden et al. 2018) pop-up that helped locate each SMDET discovery in the relevant catalog data.

[19] Only covers southern hemisphere, VHS K filter: K_s.

[20] Only covers northern hemisphere, UKIDSS LAS DR9 K filter: K_{MKO}.

Table 1
Discoverer, Photometry, Astrometry, and Derived Quantities

Column Name	Column Description	Example Entry
CWISE_Name	CWISE Designation	J043918.82+134231.1
CW_RA	CWISE R.A. measurement (deg)	1.05837
CW_DEC	CWISE decl. measurement (deg)	4.73992
CW_RAerr	CWISE R.A. uncertainty measurement (deg)	0.07510
CW_DECerr	CWISE decl. Uncertainty measurement (deg)	0.07380
CW_MJD	CWISE Modified Julian Date	56700
VHS_RA	VHS R.A. measurement (deg)	…
VHS_DEC	VHS decl. measurement (deg)	…
VHS_MJD	VHS Modified Julian Date	…
LAS_RA	UKIDSS LAS DR9 R.A. measurement (deg)	1.05860
LAS_DEC	UKIDSS LAS DR9 decl. measurement (deg)	4.74035
LAS_MJD	UKIDSS Modified Julian Date	55187
UHS_RA	UHS R.A. measurement (deg)	…
UHS_DEC	UHS decl. measurement (deg)	…
UHS_MJD	UHS Modified Julian Date	…
PS_RA	PanSTARRS DR2 R.A. measurement (deg)	1.05841
PS_DEC	PanSTARRS DR2 decl. measurement (deg)	4.73997
PS_RAerr	PanSTARRS DR2 R.A. uncertainty measurement (deg)	0.12252
PS_DECerr	PanSTARRS DR2 decl. uncertainty measurement (deg)	0.12252
PS_MJD	PanSTARRS DR2 Modified Julian Date	56873
Discover	Object Discoverers	Yadukrishna Raghu, …
W1	W1-band magnitude from CatWISE2020 (mag)	14.873
W1err	Uncertainty in W1, as provided by CatWISE2020 (mag)	0.017
W2	W2-band magnitude from CatWISE2020 (mag)	14.647
W2err	Uncertainty in W2, as provided by CatWISE2020 (mag)	0.024
W3	W3-band magnitude from AllWISE (mag)	11.777
W3err	Uncertainty in W3, as provided by AllWISE (mag)	…
W4	W4-band magnitude from AllWISE (mag)	8.621
W4err	Uncertainty in W4, as provided by AllWISE (mag)	…
J	J-band magnitude from VHS/UKIDSS LAS DR9 (mag)	16.800
Jerr	Uncertainty in J, as provided by VHS/UKIDSS LAS DR9 (mag)	0.019
Kmko	$K_{\rm MKO}$-band magnitude from UKIDSS LAS DR9 (mag)	15.609
Kmkoerr	Uncertainty in $K_{\rm MKO}$, as provided by UKIDSS LAS DR9 (mag)	0.022
Ks	K_s-band magnitude from VHS (mag)	…
Kserr	Uncertainty in K_s, as provided by VHS (mag)	…
r	r-band magnitude from PanSTARRS DR2 (mag)	…
rerr	Uncertainty in r, as provided by PanSTARRS DR2 (mag)	…
i	i-band magnitude from PanSTARRS DR2 (mag)	…
ierr	Uncertainty in i, as provided by PanSTARRS DR2 (mag)	…
z	z-band magnitude from PanSTARRS DR2 (mag)	20.069
zerr	Uncertainty in z, as provided by PanSTARRS DR2 (mag)	0.028
y	y-band magnitude from PanSTARRS DR2 (mag)	18.867
yerr	Uncertainty in y, as provided by PanSTARRS DR2 (mag)	0.034
CW_PMRA	Proper motion in R.A., as provided by CatWISE2020 (arcsec yr^{-1})	0.321
CW_PMRAerr	Uncertainty in PMRA, as provided by CatWISE2020 (arcsec yr^{-1})	0.013
CW_PMDec	Proper motion in decl., as provided by CatWISE2020 (arcsec yr^{-1})	0.134
CW_PMDecerr	Uncertainty in PMDec, as provided by CatWISE2020 (arcsec yr^{-1})	0.013
CW_PMTot	Total proper motion, as provided by CatWISE2020 (arcsec yr^{-1})	0.348
CW_PMToterr	Uncertainty in total proper motion, as provided by CatWISE2020 (arcsec yr^{-1})	0.018
PMRA	Proper motion in R.A., as described in Section 3 (arcsec yr^{-1})	−0.166
PMRAerr	Uncertainty in PMRA, as described in Section 3 (arcsec yr^{-1})	0.039
PMDec	Proper motion in decl., as described in Section 3 (arcsec yr^{-1})	−0.321
PMDecerr	Uncertainty in PMDec, as described in Section 3 (arcsec yr^{-1})	0.061
PMTot	Total proper motion, as described in Section 3 (arcsec yr^{-1})	0.362
PMToterr	Uncertainty in total proper motion, as described in Section 3 (arcsec yr^{-1})	0.057
SpT	Derived estimated photometric spectral type from Section 4.1	L3
SpT_spec	Derived spectral type from observed spectrum in Section 4.2	…
chi2	Derived χ^2 value from Section 4.1	5.660
distance	Derived distance from Section 5(pc)	64.820
distance_err	Uncertainty in distance, as derived from Section 5 (pc)	2.890
vtan	Derived $V_{\rm tan}$ from Section 5 (km s^{-1})	106.809
vtan_err	Uncertainty in $v$tan, as derived from Section 5 (km s^{-1})	7.356

Note. This table only describes the columns in the full table. The full table is available from the journal.

(This table is available in its entirety in machine-readable form in the online article.)

Using WRAP, we collected R.A., decl., and modified Julian date (MJD) measurements from CatWISE2020, VHS, UKIDSS LAS DR9, UHS, and PanSTARRS DR2 for each object. We then fit a linear regression line to these measurements to determine the proper motions and associated uncertainties for each object. Due to the lack of R.A. and decl. uncertainties in

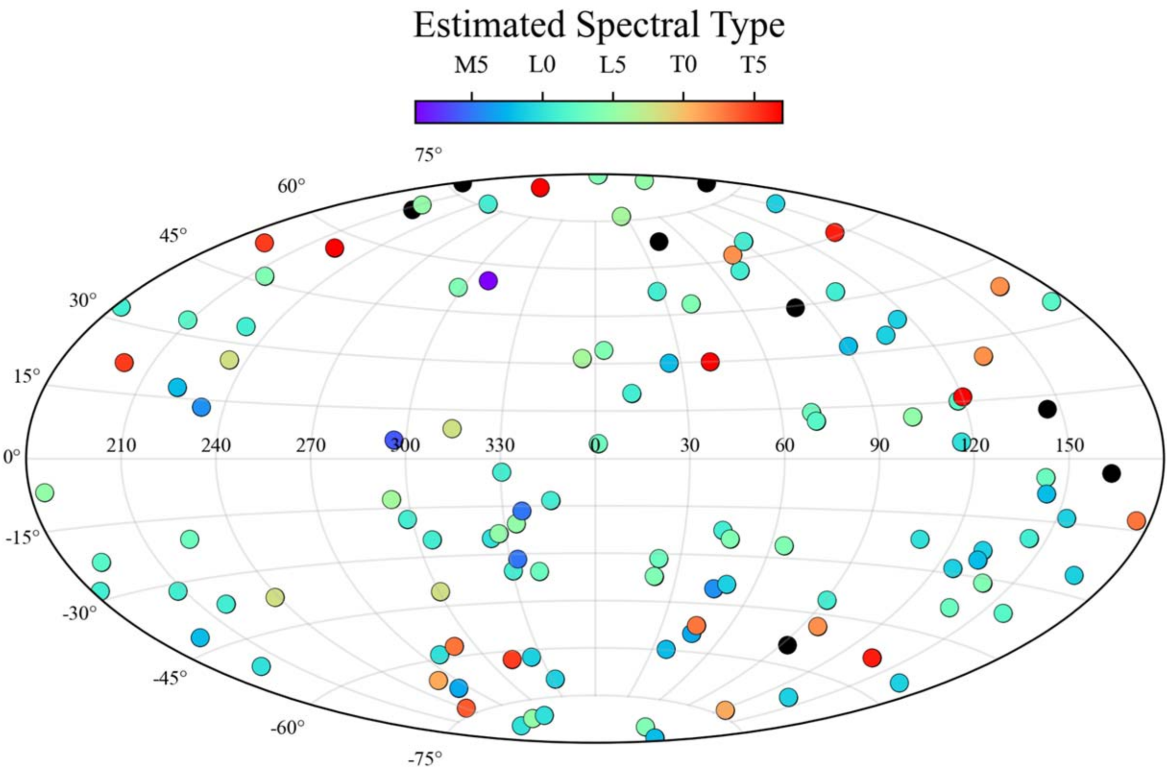

Figure 1. All-sky distribution of the 124 new `SMDET` discoveries in equatorial coordinates with the Aitoff projection. Sources are color-coded based on spectral-type estimates from Section 4, while those with a black interior are either candidate subdwarfs discussed in Section 6 or lack a photometric spectral-type estimate.

VHS, UKIDSS LAS DR9, and UHS, we required a minimum of three data points per object to obtain proper motions and their uncertainties. For objects with insufficient data points, we relied on CatWISE2020 astrometric data, as our candidates were initially discovered using WISE W1 and W2 imaging. All astrometric data is provided in Table 1.

One object, CWISE J024822.37+674812.6 (hereafter, J0248+6748), stood out as interesting but lacked *J*-band photometry, leading us to gather *J*-band photometry using the Wide-field InfraRed Camera (hereafter, WIRC; J. C. Wilson et al. 2003) on the Palomar 200″ telescope. The target was observed on 2022 July 26 (UT), with clear skies, no clouds, and a seeing full width at half maximum (FWHM) of 4 pixels (1″). The total integration time was 30 minutes, divided into 2 minute exposures obtained with a 15 point dithering pattern. Each 2 minute exposure is further divided into four frames of 30 s each. WIRC has a pixel scale of 0.″2487 per pixel and a total field of view of 8.′7 × 8.′7. The data were reduced using custom scripts written in the Interactive Data Language[21] that included dark subtraction, flat fielding, sky subtraction, and image stacking for the final mosaic. The mosaic was astrometrically and photometrically calibrated using stars from 2MASS (M. F. Skrutskie et al. 2006). Aperture photometry was performed on J0248+6748 using an aperture of 6.5 pixels (1.″6), ∼1.5 times the seeing FWHM.

Figure 2 is a compilation of color–color and color-reduced proper motion diagrams, with PanSTARRS 3π survey objects (W. M. J. Best et al. 2018) shown as colored data points in the background. Reduced proper motion at W2 ($H_{\rm W2}$) is a stand-in for absolute brightness in the absence of measured trigonometric parallaxes, and is defined as

$$\begin{aligned} H_{\rm W2} &= {\rm W2} + 5 \times \log_{10}(\mu_{\rm total}) + 5 \\ &= M_{\rm W2} + 5 \times \log_{10}(V_{\rm tan}) + 1.62, \end{aligned} \quad (1)$$

where W2 and $M_{\rm W2}$ are measured in magnitudes, $\mu_{\rm total}$ is measured in arcsec yr^{-1}, and $V_{\rm tan}$ is measured in km s^{-1}. We see in Figure 2 that all but three objects follow the general trend from W. M. J. Best et al. (2018). The three outliers, marked with numbers, are later discussed in Section 6.

4. Spectral-type Estimates

4.1. Photo-type Spectral-type Estimation Method

Spectral types can be estimated from photometry using the photo-type spectral-type estimation technique defined in N. Skrzypek et al. (2015, 2016). The method calculates the inverse variance-weighted difference between observed and empirical template colors as a function of spectral subtype:

$$\hat{m}_{B,t} = \frac{\sum_{b=1}^{N_b} \frac{\hat{m}_b - c_{b,t}}{\sigma_b^2}}{\sum_{b=1}^{N_b} \frac{1}{\sigma_b^2}}. \quad (2)$$

Here, $\{t\}$ is an array of spectral types, ranging over M0-T8 in full subtype increments; $\{b\}$ is an array of N_b photometric bands as listed in Section 3; B is the reference band, chosen as $J_{\rm MKO}$; $\hat{m}_b \pm \sigma_b$ are the measured magnitudes and uncertainties; $c_{b,t}$ are the empirical spectral subtype template color, defined as $m_b - J_{\rm MKO}$ and drawn from N. Skrzypek et al. (2015); and $\hat{m}_{B,t}$ is the averaged synthetic $J_{\rm MKO}$ apparent magnitude at each spectral subtype.

[21] https://www.nv5geospatialsoftware.com/Products/IDL

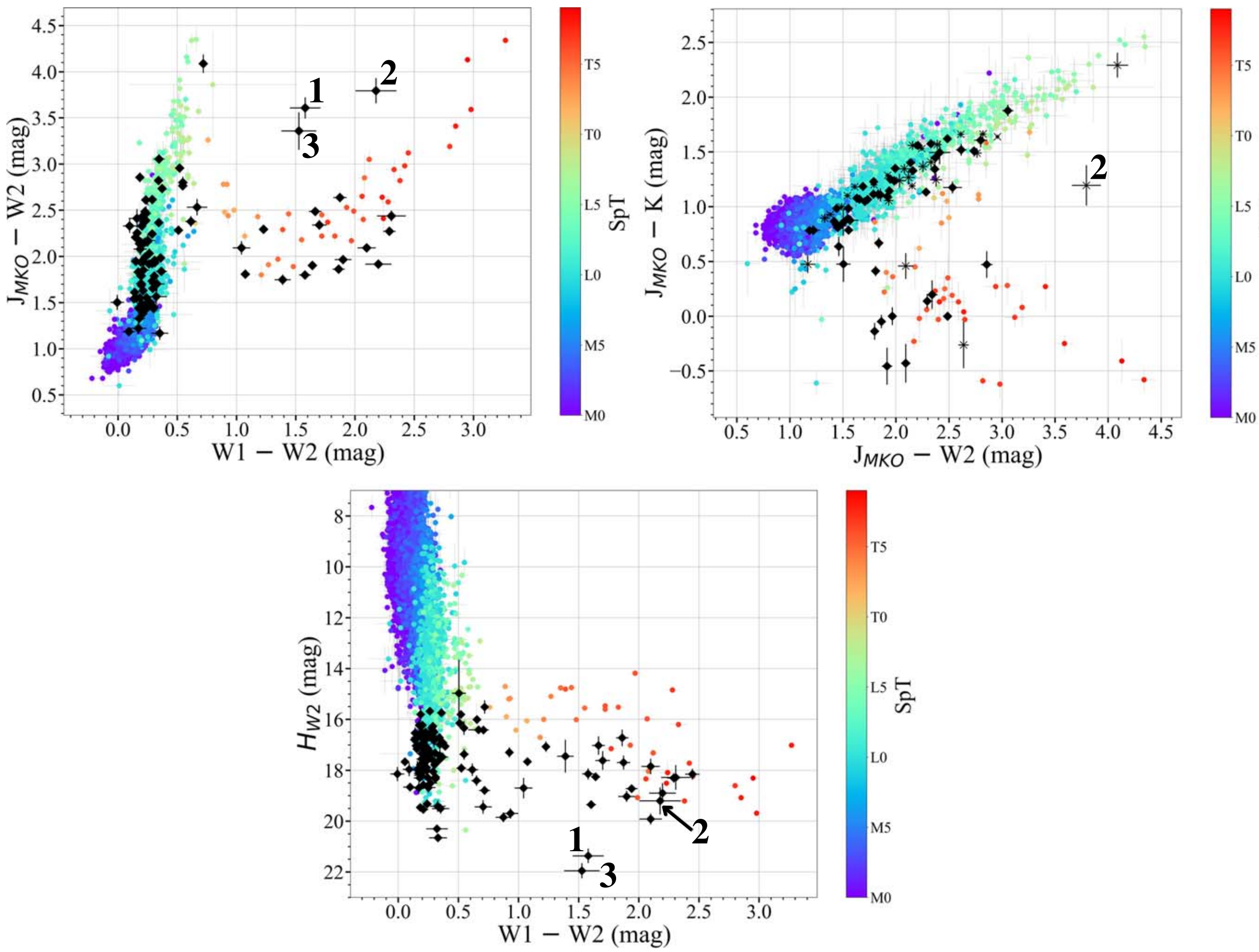

Figure 2. Color–color and reduced magnitude–color diagrams for SMDET discoveries (black points) and known ultracool dwarfs (colored data points) from the PanSTARRS 3π survey (W. M. J. Best et al. 2018). Objects from VHS and observed with the K_s filter are marked as X symbols. Objects from UKIDSS LAS DR9 and observed with the $K_{\rm MKO}$ filter are marked as diamond symbols. Points associated with numbers refer to subdwarf candidates discussed in Section 6, and correspond to 1: CWISE J024822.37+674812.6, 2: CWISE J052544.47+443409.9, and 3: CWISE J120642.54+762641.6.

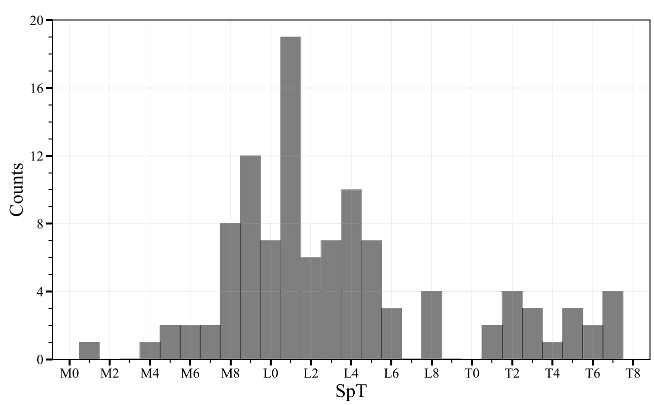

Figure 3. Distribution of spectral-type estimates for our SMDET sample. This figure does not include subdwarf candidates discovered in this paper.

The best spectral-type match was inferred using a χ^2 statistic,

$$\chi^2(\{\hat{m}_b\}, \{\sigma_b\}, \hat{m}_{B,t}, t) = \sum_{b=1}^{N_b} \left(\frac{\hat{m}_b - \hat{m}_{B,t} - c_{b,t}}{\sigma_b^2} \right)^2 \qquad (3)$$

where lower χ^2 indicates better matches. This methodology is further detailed in Appendix A of N. Skrzypek et al. (2015). S.-Y. Tang et al. (2018) further developed this method into a Python package, phot-d, which was provided to the authors (S.-Y. Tang 2022, private communication). The package use spectral type-magnitude templates from M. J. Pecaut & E. E. Mamajek (2013) for B2 to M4, W. M. J. Best et al. (2018) for M6 to L9, and N. Skrzypek et al. (2015) for T0 to T8. Note that M5 is missing in the template set. Due to the absence of Y dwarfs in these data sets, we regard any object exhibiting a color of W1 – W2 > 3.0 mag as a Y-dwarf candidate (Figure 17(h) of J. D. Kirkpatrick et al. 2021), although no such candidates were identified in our search. Note that spectral-type uncertainties were not calculated, thus they were assumed to be ideal.

Of the 118 candidates in our sample, 110 have spectral-type estimates from this technique; these are listed in Table 1, and their distribution is displayed in Figure 3. Out of the 110 photometric spectral-type estimates, six objects were found to have spectral types earlier than M7, indicating they are not ultracool dwarfs (M7 and later). Additionally, the five objects without spectral-type estimates have a W1 – W2 (mag) color between 0.55 and 0.71, which suggests they may be late-L dwarfs (J. D. Kirkpatrick et al. 2021). Lastly, three objects were discovered to be candidate subdwarfs and are later discussed in

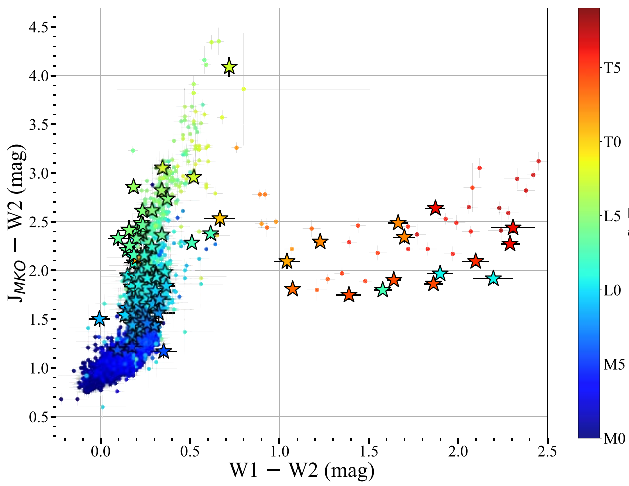

Figure 4. A color–color diagram illustrating our photo-type spectral-type estimates compared to known spectral types from W. M. J. Best et al. (2018). The starred objects are the 89 with available J_{MKO} out of 110 photo-type spectral estimates from this study.

Section 6. Spectroscopic observations are necessary for all objects in this study to confirm their estimated spectral types.

The validity of our photometric classifications is illustrated in Figure 4, which maps the spectral types of both the SMDET sample and the W. M. J. Best et al. (2018) sample on a W1 − W2 (mag) versus J − W2 (mag) diagram. The photometric classifications align well with spectral types for most of the sample, but for some late-type T dwarfs the photometric classifications are up to a full class too early. Further spectral analysis is needed to determine why these sources show such large deviations between classification methods.

4.2. Observed Candidate Spectra

We acquired spectra for two objects, CWISE J125247.68+522015.5 (hereafter, J1252+5220) and CWISE J160347.72−732054.3 (hereafter, J1603−7320), to validate our spectral-type estimates. These sources have photometric classifications of T5 and T4, respectively.

We observed J1252+5220 on the night of 2019 January 22 (UT) under good conditions with clear skies using the SpeX spectrograph J. T. Rayner et al. (2003) on NASA's IRTF telescope. These data were taken in prism mode using the 0″.8 slit to achieve a resolving power of ∼75 over the 0.8–2.5 μm wavelength range. We obtained 6 AB nods using 180 s exposures on the target and then acquired the A0 star HD 99966 for telluric correction using 0.1 s exposures and 10 AB nods. All data were reduced using the Spextool package (M. C. Cushing et al. 2004) with telluric correction and flux calibration of the A0 star following the technique described in W. D. Vacca et al. (2003).

We observed J1603−7320 on the night of 2018 April 1 (UT) under good conditions with clear skies from the Astronomy Research using the Cornell Infrared Imaging Spectrograph (ARCoIRIS; J. C. Wilson et al. 2004) on the 4 m Blanco telescope located at the Cerro Tololo Inter-American Observatory. ARCoIRIS takes simultaneous spectra across six cross-dispersed orders covering the 0.8–2.4 μm range, with a resolving power of ∼3500 using the 1″.0 slit. We obtained two different nod positions across the slit and acquired 8 AB exposures of 180 s each. After taking science exposures, we obtained nine calibration lamp images followed by an A0 star, HD 149954, for telluric correction by taking 8 AB exposure nodes of 10 s each. All data were reduced similarly to above.

We visually fit the spectral templates from A. J. Burgasser et al. (2006b), with data from A. J. Burgasser et al. (2004) and A. J. Burgasser et al. (2006a), to our measured spectra. These data provide spectroscopic classifications of T5 for J1252+5220 and T3 for J1603−7320, matching the photometric estimates within one subtype (Figure 5). Although a larger sample of spectra needs to be gathered to verify classifications over a wider range of types, these two examples provide a promising example of validation.

5. Distance and Tangential Velocity Estimates

The photo-type code uses absolute magnitudes for its empirical templates, and these can be used to estimate distances for our sources and their associated uncertainties. We used the M_{W2} empirical absolute magnitudes and W2 measured magnitudes to calculate distances, ignoring reddening effects, which are provided in Table 1. Using a standard error propagation equation, the associated uncertainties were derived from absolute magnitude template errors combined with apparent magnitude errors. Figure 6 displays J_{MKO} − W2 (mag) versus estimated distance (pc), demonstrating the expected trend wherein objects with later spectral types are only seen if they are closer to the Sun due to the photometric detection limit of WISE.

With the estimated distances and measured proper motions (where calculated proper motions were used when possible), we calculated tangential velocity (V_{tan}) estimates, also provided in Table 1. Figure 7 compares apparent W2 (mag) versus V_{tan} (km s^{-1}). The tangential velocity uncertainties were calculated using standard error propagation, errors from the total proper motion, and distance. Some of the tangential velocities are extremely high, exceeding the escape velocity of the Milky Way (H. H. Koppelman & A. Helmi 2021), albeit with large uncertainties. Measured parallaxes are needed to verify these extreme velocities.

Objects CWISE J194427.98+053342.6 and CWISE J203710.21+545750.8 are excluded from Figures 6 and 7 due to their exceptionally large distances and tangential velocities estimates of 509 (pc)/2223 (km s^{-1}) and 808 (pc)/1299 (km s^{-1}), respectively, which exceed the scale intended for these figures. These extraordinarily high values should be interpreted with caution and verified through trigonometric parallax measurements.

Six objects, all of which are earlier than M7 and thus not ultracool dwarfs, either lacked reliable distance estimates or had substantial errors. These objects are J030138.04−401755.2, J153103.62+130935.2, J194427.98+053342.6, J203710.21+545750.8, J221039.79−313533.2, and J222437.97−163134.6. The discrepancies are likely due to poor fits between the template absolute magnitudes and the measured data, coming from the minimal color differences among early spectral types. To address this issue, we recalculated the distance and tangential velocity estimates for these objects using the spectral type versus absolute W2 magnitudes from Table 7 of C. Cifuentes et al. (2020). This adjustment significantly improved the estimates. Nevertheless, measured trigometric parallaxes are still necessary to verify these estimates.

6. Candidate Subdwarfs

With any kinematic selection, there is a higher probability of finding subdwarfs (M. I. Arifyanto et al. 2005). Here, we assess

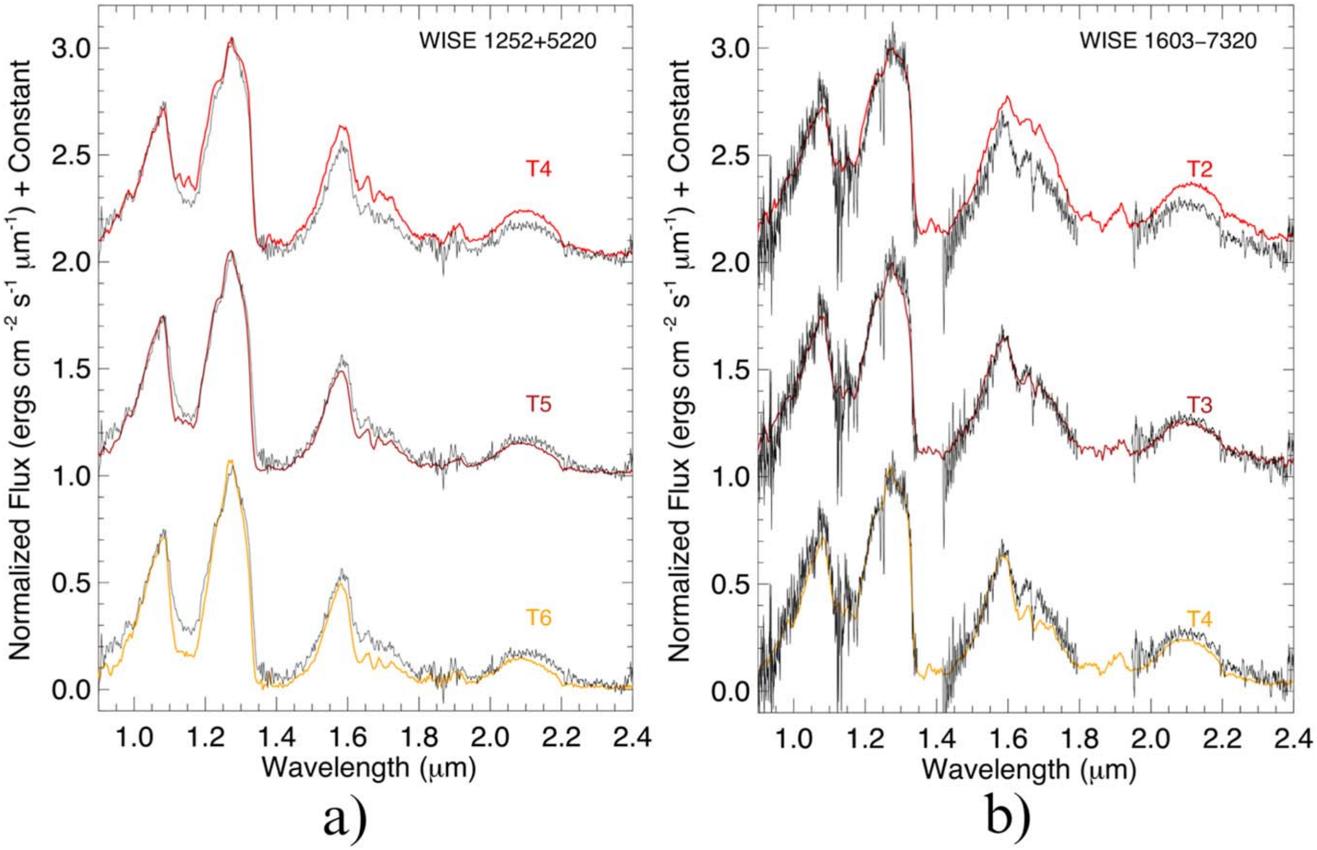

Figure 5. (a) The near-infared (0.8–2.4 μm) SpeX spectrum of J1252+5220 (black lines) compared to T4, T5, and T6 spectral standards (orange, maroon, and yellow lines, respectively). (b) Similar sequence comparing ARCoIRIS data for J1603−7320 to T2, T3, and T4 spectral standards. The standard spectra are those defined in A. J. Burgasser et al. (2006b), with data from A. J. Burgasser et al. (2004) and A. J. Burgasser et al. (2006a). All are normalized at the peak of the J bandpass (~1.3 μm).

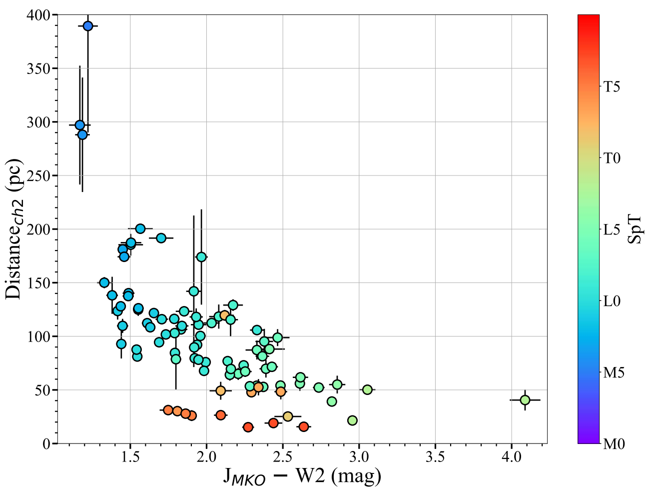

Figure 6. $J_{\rm MKO}$−W2 vs. estimated distance with associated uncertainties. Symbol color encodes photometric classifications.

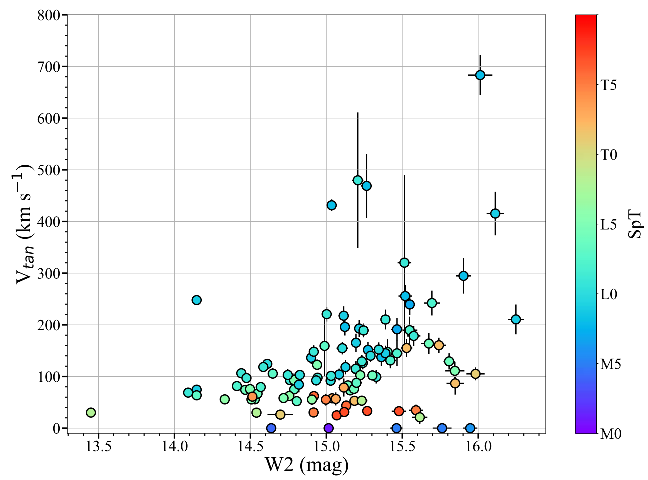

Figure 7. Apparent W2 vs. estimated tangential velocity with associated uncertainties. Symbol color encodes photometric classifications.

the presence of T subdwarfs (sdT) and extreme T subdwarfs (esdT; A. C. Schneider et al. 2020) in our sample given our focus on later-type brown dwarfs. We based our analysis on a compilation of nine color–color diagrams shown in Figure 8 of Z. H. Zhang et al. (2019), and the color–color box defined in Figure 1 of A. M. Meisner et al. (2021), to identify sdT and esdT candidates, respectively. The latter region encompasses $1.1 < \mathrm{W1} - \mathrm{W2}$ (mag) <1.75 and $J - \mathrm{W2}$ (mag) >3. We identified three possible subdwarfs, listed in Table 2.

CWISE J052544.47+443409.9 (hereafter, J0525+4434) exhibits colors akin to those of a ~sdT8? candidate reported in Figures 8(f) and (i) of Z. H. Zhang et al. (2019), which we tentatively assign as the classification of this source. J0525+4434 has a substantial proper motion of $0\farcs52 \pm 0\farcs13$ yr^{-1}. Using the $M_{\rm W2}$ reported in Z. H. Zhang et al. (2019), $M_{\rm W2} \sim 13.5$ mag, we estimate a distance of 27 pc for this source, corresponding to $V_{\rm tan} \approx 66$ km s^{-1}.

Table 2
Subdwarf Candidates

Figure 2 #	Object Name	R.A. (deg)	Decl. (deg)	SpT	M_J (mag)	Distance (pc)	V_{tan} (km s^{-1})
1	CWISE J024822.37+674812.6	42.0932152	67.8035141	esdT?	∼13	∼47	∼223
2	CWISE J052544.47+443409.9	81.4353002	44.5694241	sdT8?	∼13.5	∼27	∼66
3	CWISE J120642.54+762641.6	181.677282	76.4449143	esdT?	∼13	∼58	∼293

Two sources, CWISE J024822.37+674812.6 (hereafter, J0248+6748) and CWISE J120642.54+762641.6 (hereafter, J1206+7626) fall within the esdT region defined in A. M. Meisner et al. (2021). In the absence of spectral data, we adopt preliminary classifications of ∼esdT for both objects. Both exhibit very large proper motions of $1\farcs00 \pm 0\farcs13$ yr^{-1} and $1\farcs07 \pm 0\farcs14$ yr^{-1}, respectively. H. Brooks et al. (2022) adopt an absolute magnitude of $M_{W2} \sim 13$ mag for esdT candidates within a similar region of color–color space, implying distance estimates of ∼47 pc for J0248+6748 and ∼58 pc for J1206+7626, which in turn imply $V_{tan} \sim 223$ km s^{-1} and ∼293 km s^{-1}, respectively. Such high velocities are consistent with halo population objects; however, spectra and parallax measurements are needed to validate these measures.

7. Candidate Young Objects

Among the few sources in our sample that did not have reliable photometric classifications, but are not subdwarfs, it is possible that their deviant colors arise from having low surface gravity atmospheres. We used the BANYAN Σ Bayesian classifier (J. Gagné et al. 2018b) to examine whether any of our discoveries are candidate members of a known nearby young association. The BANYAN Σ tool uses available observational properties such as sky position, proper motion, radial velocity, and distance to assess whether a given object has *XYZ* Galactic space coordinates and *UVW* space velocities that match the location and kinematics of known young associations. In cases where a radial velocity and/or a distance is missing, these parameters can be marginalized and a membership probability can still be determined.

We used the photometric distances presented in Table 1 combined with the sky coordinates and proper motions from Table 1 to determine membership probabilities. We used the updated kinematic models of J. Gagné (2024), up to a distance of 814 pc corresponding to the largest plausible distance of our ultracool dwarf candiates at 3σ. We used a Monte Carlo approach with 10^4 samples to marginalize over the measurement errors of the proper motion, which is computationally slower but more accurate than the error propagation of proper motion otherwise done in BANYAN Σ (J. Gagné et al. 2018b). Using this method, we identified only two low-likelihood candidate members among our sample both of which lack a photometric classification.

CWISE J060938.14−542916.3 (hereafter J0609−5429) was found to be a low-probability (50%) candidate member of a nearby moving group. This probability is comprised of: 59% (equivalent to 29.5% overall) of the membership probability is assigned to the ≈300 Myr old corona of Group 23 from S. Oh et al. (2017; see L. Moranta et al. 2022 for a discussion of this structure, and M. Kounkel et al. 2020 for the age estimation of the associated structure Theia 599), and 36% (18% overall) is associated with the ≈700 Myr old (F. J. Galindo-Guil et al. 2022) Hyades tidal tail (S. Röser et al. 2019). The remaining 5% (2.5% overall) probability is assigned to the field.

CWISE J141615.86+685919.7 (hereafter J1416+6859) was found to be a high-probability (85%) candidate member of a nearby moving group. This is split between two groups: 68% (equivalent to 57.8% overall) in the ≈500–600 Myr old Oceanus moving group (J. Gagné et al. 2023), and 24% (20.4% overall) in the ≈133 Myr old AB Doradus moving group (B. Zuckerman et al. 2004; J. Gagné et al. 2018b). The remaining 8% (6.8% overall) probability is assigned to the field.

We consider both of these objects to be weak candidate members of their respective associations due to their lack of classifications, photometric distance estimates, and tangential velocity estimates, and therefore complete assessment of their *XYZ* and *UVW* kinematics. This means that the probabilities are based solely on the sky position and proper motion of these candidates. We also lack spectral evidence of youth which would be required to make them convincing members of their respective associations. Additionally, our reliance on the photometric distances for other sources in our sample could have caused us to miss members of nearby young associations if they are young enough to have atypical colors or absolute magnitudes (usually ⩽ 200 Myr; J. K. Faherty et al. 2016). Therefore, once trigonometric parallaxes are taken for these objects, the BANYAN Σ analysis should be performed again.

Alongside the BANYAN Σ calculations, we found that CWISE J153653.38+253801.9 (herafter J1536+2538) has $J-K$ and $J-$W2 colors that are extremely red for its estimated spectral type. This may be a result of youth, as young L dwarfs are known to possess redder near-infrared colors than their field-age counterparts as they are still contracting and therefore have low surface gravities. The resulting low atmospheric pressure causes reduced collision-induced absorption by H_2 (J. L. Linsky 1969) and an excess of high-altitude dust clouds in their photospheres (M. C. Cushing et al. 2008; J. K. Faherty et al. 2016), shifting emergent flux to longer wavelengths. However, BANYAN Σ indicates that J1536+2538 is not a member of a known young moving group. There is a possibility that this source is a young object that has been ejected from its natal environment. However, a population of field-age objects exists that possess red near-infrared colors (F. Marocco et al. 2014), thought to have an excess of submicron sized dust grains in their upper atmospheres (K. Hiranaka et al. 2016). Other factors are also known to redden the near-infrared colors of brown dwarfs, such as supersolar metallicity (D. L. Looper et al. 2008) and equator-on inclination angle (J. M. Vos et al. 2017; G. Suárez & S. Metchev 2022; G. Suárez et al. 2023). Consequently, spectroscopic data must be obtained for J1536+2538 for confirmation of its youth.

8. Limitations of this Study

The proper motion distribution and orientations in our sample are shown in Figure 8. This figure highlights that our sample has

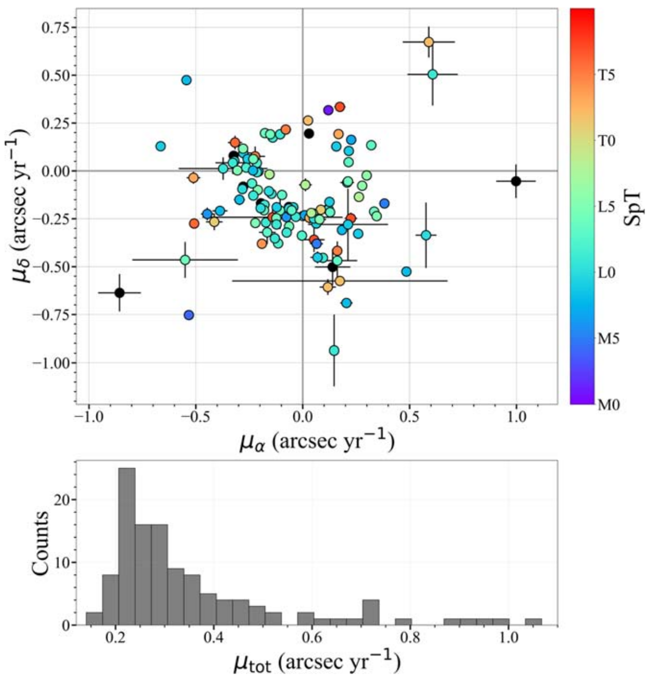

Figure 8. The top plot compares μ_α to μ_δ (arcsec yr^{-1}), with symbol color encoding photometric classification. The black points with associated numbers are subwarfs described in Section 6. The bottom plot shows the distribution of the total proper motion of the SMDET sample. Note that objects with calculated proper motions were utilized in the analysis, while all other objects relied on proper motion measurements from CatWISE2020.

a minimum detection limit for μ_{tot} (total proper motion) of about 0.2 (arcsec yr^{-1}). This is not because SMDET fails to identify low proper motion objects, rather SDMET was trained with solely high proper motion examples thus assigning low proper motion objects lower scores. Low proper motion candidates are overwhelmed by false positives that likely lead to them being overlooked during human verification. As a result, these low proper motion candidates are often overshadowed by false positives and may be overlooked during human verification. Therefore, this minimum detection limit reflects both a human bias and an inherent feature of the SMDET training process. To achieve a lower minimum proper motion detection limit, a new training set would need to be developed and run through the neural network, which future surveys should aim to accomplish.

The distribution of photometric classifications is shown in Figure 3. This figure does not include the 3 subdwarf candidates discussed in Section 6. We anticipated a bias toward later spectral types due to this study focusing on colder, fainter sources. However, our distribution suggests the opposite trend. This discrepancy can be attributed to the sensitivity limit of the photometric surveys, which restricts the volume in which each spectral type can be detected. The brighter, earlier-type dwarfs are simply detected out to a larger volume. Discovering later-type brown dwarfs at increased distances will need next-generation infrared surveys, such as the Near-Earth Object Surveyor (A. K. Mainzer et al. 2023), Nancy Grace Roman Space Telescope (N. J. Kasdin et al. 2020), Euclid (G. D. Racca et al. 2016), and others.

9. Conclusion

We report the discovery of 118 new ultracool dwarf candidates. We combined photometry and astrometry from multiple catalogs to derive estimates for spectral type, distance, and tangential velocity. Our sample includes 28 M, 64 L, and 18 T dwarfs, and we verified the spectral types of two T dwarf candidates using near-infrared spectroscopy. We also identified one new T-subdwarf and two new extreme-T-subdwarf candidates, based on their similar colors to previously confirmed subdwarfs, as well as two low-probability candidate young ultracool dwarfs.

Acknowledgments

Backyard Worlds research was supported by NASA grant 2017-ADAP17-0067 and by the NSF under grants AST-2007068, AST-2009177, and AST-2009136. This work makes use of data products from WISE/NEOWISE, which is a joint project of UCLA and JPL/Caltech, funded by NASA. The CatWISE effort was led by the Jet Propulsion Laboratory, California Institute of Technology, with funding from NASA's Astrophysics Data Analysis Program. The observations obtained as part of the VISTA Hemisphere Survey, ESO Progam, were funded by the grant 179.A-2010 (PI: McMahon). The UHS is a partnership between the UK STFC, The University of Hawaii, The University of Arizona, Lockheed Martin, and NASA.

The PanSTARRS2 Surveys (PS2) and the PS2 public science archive have been made possible through contributions by the Institute for Astronomy, the University of Hawaii, the PanSTARRS Project Office, the Max-Planck Society and its participating institutes, the Max Planck Institute for Astronomy, Heidelberg and the Max Planck Institute for Extraterrestrial Physics, Garching, The Johns Hopkins University, Durham University, the University of Edinburgh, the Queen's University Belfast, the Harvard-Smithsonian Center for Astrophysics, the Las Cumbres Observatory Global Telescope Network Incorporated, the National Central University of Taiwan, the Space Telescope Science Institute, the National Aeronautics and Space Administration under grant No. NNX08AR22G issued through the Planetary Science Division of the NASA Science Mission Directorate, the National Science Foundation grant No. AST-1238877, the University of Maryland, Eotvos Lorand University (ELTE), the Los Alamos National Laboratory, and the Gordon and Betty Moore Foundation.

This paper uses observations obtained at the Hale Telescope, at Palomar Observatory, which is part of a continuing collaboration between the California Institute of Technology, NASA/JPL, Yale University, and the National Astronomical Observatories of China.

This research has made use of the VizieR catalog access tool, CDS, Strasbourg, France (DOI:10.26093/cds/vizier). The original description of the VizieR service was published in 2000, A&AS 143, 23. This work has made use of data from the European Space Agency (ESA) mission Gaia (https://www.cosmos.esa.int/Gaia), processed by the Gaia Data Processing and Analysis Consortium (DPAC; https://www.cosmos.esa.int/web/Gaia/dpac/consortium). Funding for the DPAC has been provided by national institutions, in particular, the institutions participating in the Gaia Multilateral Agreement.

Software: WiseView (D. Caselden et al. 2018), SpeXTool (M. C. Cushing et al. 2004), Matplotlib (J. D. Hunter 2007), NumPy (S. van der Walt et al. 2011).

ORCID iDs

Hunter Brooks https://orcid.org/0000-0002-5253-0383
Dan Caselden https://orcid.org/0000-0001-7896-5791
J. Davy Kirkpatrick https://orcid.org/0000-0003-4269-260X

Yadukrishna Raghu https://orcid.org/0000-0001-9778-7054
Jake Grigorian https://orcid.org/0000-0002-2466-865X
Asa Trek https://orcid.org/0009-0008-3778-487X
Andrew Washburn https://orcid.org/0009-0005-6222-6026
Hiro Higashimura (東村滉) https://orcid.org/0009-0004-9088-7510
Aaron M. Meisner https://orcid.org/0000-0002-1125-7384
Adam C. Schneider https://orcid.org/0000-0002-6294-5937
Jacqueline K. Faherty https://orcid.org/0000-0001-6251-0573
Federico Marocco https://orcid.org/0000-0001-7519-1700
Christopher R. Gelino https://orcid.org/0000-0001-5072-4574
Jonathan Gagné https://orcid.org/0000-0002-2592-9612
Thomas P. Bickle https://orcid.org/0000-0003-2235-761X
Shih-Yun Tang https://orcid.org/0000-0003-4247-1401
Austin Rothermich https://orcid.org/0000-0003-4083-9962
Adam J. Burgasser https://orcid.org/0000-0002-6523-9536
Marc J. Kuchner https://orcid.org/0000-0002-2387-5489
Guillaume Colin https://orcid.org/0000-0002-7630-1243
Giovanni Colombo https://orcid.org/0000-0002-8295-542X
Leopold Gramaize https://orcid.org/0000-0002-8960-4964
Les Hamlet https://orcid.org/0000-0002-7389-2092
Ken Hinckley https://orcid.org/0000-0002-4733-4927
Martin Kabatnik https://orcid.org/0000-0003-4905-1370
Frank Kiwy https://orcid.org/0000-0001-8662-1622
Arttu Sainio https://orcid.org/0000-0003-4864-5484
Jörg Schümann https://orcid.org/0000-0002-7587-7195
Nikolaj Stevnbak https://orcid.org/0000-0003-4714-3829
Melina Thévenot https://orcid.org/0000-0001-5284-9231

References

Arifyanto, M. I., Fuchs, B., Jahreiß, H., et al. 2005, A&A, 433, 911
Best, W. M. J., Dupuy, T. J., Liu, M. C., Siverd, R. J., & Zhang, Z. 2020, The UltracoolSheet: Photometry, Astrometry, Spectroscopy, and Multiplicity for 3000+ Ultracool Dwarfs and Imaged Exoplanets, v1.0.0, Zenodo, doi:10.5281/zenodo.4169085
Best, W. M. J., Magnier, E. A., Liu, M. C., et al. 2018, ApJS, 234, 1
Bihain, G., & Scholz, R.-D. 2016, A&A, 589, A26
Brooks, H., Kirkpatrick, J. D., Caselden, D., et al. 2022, AJ, 163, 47
Brooks, H., Kirkpatrick, J. D., Caselden, D., et al. 2023, RNAAS, 7, 272
Burgasser, A. J., Burrows, A., & Kirkpatrick, J. D. 2006a, ApJ, 639, 1095
Burgasser, A. J., Geballe, T. R., Leggett, S. K., Kirkpatrick, J. D., & Golimowski, D. A. 2006b, ApJ, 637, 1067
Burgasser, A. J., McElwain, M. W., Kirkpatrick, J. D., et al. 2004, AJ, 127, 2856
Caselden, D., Colin, G., Lack, L., et al. 2020, BAAS, 52, 1
Caselden, D., Westin, P., Meisner, A., Kuchner, M., & Colin, G., 2018 WiseView: Visualizing motion and variability of faint WISE sources, Astrophysics Source Code Library, ascl:1806.004
Chambers, K. C., Magnier, E. A., Metcalfe, N.>, et al. 2016, arXiv:1612.05560
Cifuentes, C., Caballero, J. A., Cortés-Contreras, M., et al. 2020, A&A, 642, A115
Cross, N. J. G., Collins, R. S., Mann, R. G., et al. 2012, A&A, 548, A119
Cushing, M. C., Kirkpatrick, J. D., Gelino, C. R., et al. 2011, ApJ, 743, 50
Cushing, M. C., Marley, M. S., Saumon, D., et al. 2008, ApJ, 678, 1372
Cushing, M. C., Vacca, W. D., & Rayner, J. T. 2004, PASP, 116, 362
Cutri, R. M., Wright, E. L., Conrow, T., et al. 2021, yCat, II/328
Dantona, F., & Mazzitelli, I. 1986, A&A, 162, 80
Dye, S., Lawrence, A., Read, M. A., et al. 2018, MNRAS, 473, 5113
Faherty, J. K., Burgasser, A. J., Cruz, K. L., et al. 2009, AJ, 137, 1
Faherty, J. K., Gagne, J., Weinberger, A., et al. 2021, BAAS, 53, 1
Faherty, J. K., Riedel, A. R., Cruz, K. L., et al. 2016, ApJS, 225, 10
Gagné, J. 2024, PASP, 136, 063001
Gagné, J., Fontaine, G., Simon, A., et al. 2018b, ApJL, 861, L13
Gagné, J., Moranta, L., Faherty, J. K., et al. 2023, ApJ, 945, 119
Gaia Collaboration, Vallenari, A., & Brown, A. G. A. 2023, A&A, 674, A1
Galindo-Guil, F. J., Barrado, D., Bouy, H., et al. 2022, A&A, 664, A70
Greco, J. J., Cushing, M., Mace, G., Metchev, S., & Marley, M. 2020, BAAS, 52, 1
Hiranaka, K., Cruz, K. L., Douglas, S. T., et al. 2016, ApJ, 830, 96
Hunter, J. D. 2007, CSE, 9, 90
Kasdin, N. J., Bailey, V. P., Mennesson, B., et al. 2020, Proc. SPIE, 11443, 114431U
Kirkpatrick, J. D., Cushing, M. C., Gelino, C. R., et al. 2011, ApJS, 197, 19
Kirkpatrick, J. D., Gelino, C. R., Faherty, J. K., et al. 2021, ApJS, 253, 7
Kirkpatrick, J. D., Kellogg, K., Schneider, A. C., et al. 2016, ApJS, 224, 36
Kirkpatrick, J. D., Schneider, A., Fajardo-Acosta, S., et al. 2014, ApJ, 783, 122
Koppelman, H. H., & Helmi, A. 2021, A&A, 649, A136
Kota, T., Kirkpatrick, J. D., Caselden, D., et al. 2022, AJ, 163, 116
Kounkel, M., Covey, K., & Stassun, K. G. 2020, AJ, 160, 279
Kuchner, M. J., Faherty, J. K., Schneider, A. C., et al. 2017, ApJL, 841, L19
Lawrence, A., Warren, S. J., Almaini, O., et al. 2007, MNRAS, 379, 1599
Linsky, J. L. 1969, ApJ, 156, 989
Looper, D. L., Kirkpatrick, J. D., Cutri, R. M., et al. 2008, ApJ, 686, 528
Luhman, K. L. 2014, ApJ, 781, 4
Mainzer, A. K., Masiero, J. R., Abell, P. A., et al. 2023, PSJ, 4, 224
Marocco, F., Day-Jones, A. C., Lucas, P. W., et al. 2014, MNRAS, 439, 372
Marocco, F., Eisenhardt, P. R. M., Fowler, J. W., et al. 2021, ApJS, 253, 8
Meisner, A. M., Caselden, D., Kirkpatrick, J. D., et al. 2020a, ApJ, 889, 74
Meisner, A. M., Lang, D., & Schlegel, D. J. 2018, AJ, 156, 69
Meisner, A. M., Schneider, A. C., Burgasser, A. J., et al. 2021, ApJ, 915, 120
Moranta, L., Gagné, J., Couture, D., et al. 2022, ApJ, 939, 94
Oh, S., Price-Whelan, A. M., Hogg, D. W., et al. 2017, AJ, 153, 257
Pecaut, M. J., & Mamajek, E. E. 2013, ApJS, 208, 9
Racca, G. D., Laureijs, R., Stagnaro, L., et al. 2016, Proc. SPIE, 9904, 99040O
Rayner, J. T., Toomey, D. W., Onaka, P. M., et al. 2003, PASP, 115, 362
Röser, S., Schilbach, E., & Goldman, B. 2019, A&A, 621, L2
Schneider, A. C., Burgasser, A. J., Gerasimov, R., et al. 2020, ApJ, 898, 77
Schneider, A. C., Greco, J., Cushing, M. C., et al. 2016, ApJ, 817, 112
Skrutskie, M. F., Cutri, R. M., Stiening, R., et al. 2006, AJ, 131, 1163
Skrzypek, N., Warren, S. J., & Faherty, J. K. 2016, A&A, 589, A49
Skrzypek, N., Warren, S. J., Faherty, J. K., et al. 2015, A&A, 574, A78
Suárez, G., & Metchev, S. 2022, MNRAS, 513, 5701
Suárez, G., Vos, J. M., Metchev, S., et al. 2023, ApJL, 954, L6
Tang, S.-Y., Chen, W. P., Chiang, P. S., et al. 2018, ApJ, 862, 106
Vacca, W. D., Cushing, M. C., & Rayner, J. T. 2003, PASP, 115, 389
van der Walt, S., Colbert, S. C., & Varoquaux, G. 2011, CSE, 13, 22
Vos, J. M., Allers, K. N., & Biller, B. A. 2017, ApJ, 842, 78
Wenger, M., Ochsenbein, F., Egret, D., et al. 2000, A&AS, 143, 9
Wilson, J. C., Eikenberry, S. S., Henderson, C. P., et al. 2003, Proc. SPIE, 4841, 451
Wilson, J. C., Henderson, C. P., Herter, T. L., et al. 2004, Proc. SPIE, 5392, 1295
Wright, E. L., Eisenhardt, P. R. M., Mainzer, A. K., et al. 2010, AJ, 140, 1868
Zhang, Z. H., Burgasser, A. J., Gálvez-Ortiz, M. C., et al. 2019, MNRAS, 486, 1260
Zuckerman, B., Song, I., & Bessell, M. S. 2004, ApJL, 613, L65